BRÜCKNER, S. (1982). *Acta Cryst.* B**38**, 2405–2408.
CHERNIKOVA, N. YU., BELSKY, V. K. & ZORKY, P. M. (1990). *Russ. J. Struct. Chem.* **31**, 661–666.
CHERNIKOVA, N. YU. & ZORKY, P. M. (1979). *Russ. J. Struct. Chem.* **20**, 384–389.
CURTIS, C. W. & REINER, I. (1962). *Representation Theory of Finite Groups and Associative Algebras*. New York/London: John Wiley.
International Tables for X-ray Crystallography (1974). Vol. IV. Birmingham: Kynoch Press. (Present distributor Kluwer Academic Publishers, Dordrecht.)
KITAIGORODSKII, A. I. (1961). *Organic Chemical Crystallography*. New York: Consultants Bureau.
KITAIGORODSKII, A. I. (1973). *Molecular Crystals and Molecules*. New York: Academic Press.
KITAIGORODSKII, A. I., ZORKY, P. M. & BELSKY, V. K. (1980). *Stroenie Organicheskogo Veshchestva. Dannye Strukturnykh Issledovanii* 1929–1970 (*The Structure of Organic Substances. The Data of Structural Studies* 1929–1970). Moscow: Nauka.
KITAIGORODSKII, A. I., ZORKY, P. M. & BELSKY, V. K. (1982). *Stroenie Organicheskogo Veshchestva. Dannye Strukturnykh Issledovanii* 1971–1973 (*The Structure of Organic Substances. The Data of Structural Studies* 1971–1973). Moscow: Nauka.
KITAIGORODSKII, A. I., ZORKY, P. M. & BELSKY, V. K. (1984). *Stroenie Organicheskikh i Elementoorganicheskikh Molekul. Bibliograficheskii Ukazatel* 1929–1979 (*The Structure of Organic and Elementorganic Molecules. Bibliographical Index for* 1929–1979). Moscow: Nauka.
KONDRASHEV, YU. D. & ANDREEVA, N. A. (1963). *Zh. Strukt. Khim.* **4**, 454–457.
MORNON, J.-P., BALLY, R. & BRASSY, C. (1977). *C. R. Acad. Sci.* C**284**, 779–781.
PADMAYA, N., RAMAKUMAR, S. & VISWAMITRA, M. A. (1990). *Acta Cryst.* A**46**, 725–730.
PRAGER, B., STERN, D. & ILBERG, K. (1929). *System der organischen Verbindungen* (*Ein Leitfaden fur die Benutzung von Beilsteins Handbuch*). Berlin: Springer.
PROKHVATILOV, A. I. & ISAKINA, A. P. (1980). *Acta Cryst.* B**36**, 1576–1580.
PUFF, H., BRAUN, K. & REUTER, H. (1991). *J. Organomet. Chem.* **409**, 119–129.
RÜTHERFORD, J. S. & CALVO, C. (1969). *Z. Kristallogr.* **128**, 229.
SCARINGE, R. P. (1991). *Electron Crystallography of Organic Molecules*, pp. 85–113. Dordrecht: Kluwer.
SENECHAL, M. (1975). *Z. Kristallogr.* **142**, 1–23.
SHIEH, H. S., HOARD, L. G. & NORDMAN, C. E. (1977). *Nature* (*London*), **267**, 287–289.
SHIEH, H. S., HOARD, L. G. & NORDMAN, C. E. (1981). *Acta Cryst.* B**37**, 1538–1543.
WILSON, A. J. C. (1988). *Acta Cryst.* A**44**, 715–724.
WILSON, A. J. C. (1990). *Acta Cryst.* A**46**, 742–754.
WILSON, A. J. C. (1991). *Z. Kristallogr.* **197**, 85–88.
WILSON, A. J. C. (1993). *Acta Cryst.* A**49**, 795–806.
WONDRATSCHEK, H. (1976). *Z. Kristallogr.* **143**, 460–470.
YAMAGUCHI, K., OHSAWA, A., ITOH, T. & KAWABATA, C. (1988). *J. Pharm. Soc. Jpn*, **108**, 1040–1045.
ZORKY, P. M. (1968). *Kristallografiya*, **13**, 26–32.
ZORKY, P. M. (1982). *Fizicheskaya Khimiya. Sovremennye Problemy* (*Physical Chemistry. The Modern Problems*), pp. 134–178. Moscow: Khimiya.
ZORKY, P. M. (1991). XIII European Crystallography Meeting, Trieste, Book of Abstracts, p. 11.
ZORKY, P. M. & BELSKY, V. K. (1972). *Zh. Strukt. Khim.* **13**, 305–308.
ZORKY, P. M., BELSKY, V. K., LAZAREVA, S. G. & PORAI-KOSHITS, M. A. (1967). *Zh. Strukt. Khim.* **8**, 312–316.
ZORKY, P. M. & CHERNIKOVA, N. YU. (1985). *Itogi Nauki Tekh. Kristallokhim.* **19**, 237–279.
ZORKY, P. M. & DASHEVSKAYA, E. E. (1992). *Russ. J. Phys. Chem.* **66**, 35–42.
ZORKY, P. M. & KUKINA, T. N. (1981). *Vestn. Mosk. Univ. Ser. Khim.* **22**, 137–140.
ZORKY, P. M. & NESTEROVA, YA. M. (1986). *Russ. J. Struct. Chem.* **27**, 103–106.
ZORKY, P. M. & NESTEROVA, YA. M. (1990). *Russ. J. Struct. Chem.* **31**, 940–942.
ZORKY, P. M. & NESTEROVA, YA. M. (1993). *Russ J. Phys. Chem.* **67**, 195–198.
ZORKY, P. M., POTEKHIN, K. A. & DASHEVSKAYA, E. E. (1993). *Acta Chim. Hung.* **130**, 221–233.
ZORKY, P. M., RAZUMAEVA, A. E. & BELSKY, V. K. (1977). *Acta Cryst.* A**33**, 1001–1004.

Acta Cryst. (1995). A**51**, 481–489

Microdiffraction and CBED Crystal Structure Determination of the Si-Rich Phase in Laser-Clad Ni Alloy FP-5

BY Y. LIU* AND J. MAZUMDER

Center for Laser Aided Material Processing, Department of Mechanical and Industrial Engineering, University of Illinois at Urbana-Champaign, 1206 West Green Street, Urbana, IL 61801, USA

(*Received* 15 *August* 1994; *accepted* 25 *November* 1994)

Abstract

This paper demonstrates an example of using kinematical microdiffraction to solve an unknown Si-rich phase of micrometer size in a laser-clad Ni alloy FP-5 on Al alloy AA333. The composition of the Si-rich phase obtained by energy-dispersive X-ray spectroscopy (EDX) analysis in a transmission electron microscope is approximately 0.7wt% Al, 71wt% Si, 3.3wt% Cr, 0.8wt% Fe, 21wt% Ni and 2.7wt% Cu. The point group was identified by the standard convergent-beam symmetry analysis to be $P6_3/mmc$ (No. 194). Structure analysis by microdiffraction (MD) indicates that the Si-rich phase is a close-

*Current address: Department of Mechanical Engineering, University of Nebraska-Lincoln, 255 Walter Scott Engineering Center, Lincoln, NE 68588-0656, USA.

packed structure. The intensity distribution in the microdiffraction pattern of the [11$\bar{2}$0] zone axis taken with a very thin area showed a close match with kinematical calculation. A close-packed-structure model specified as *ABCACB* was deduced from the [11$\bar{2}$0] zone-axis MD pattern. The randomly distributed atoms of all the elements in the unit cell are at $\frac{2}{3}, \frac{1}{3}, -\frac{1}{12}; \frac{1}{3}, \frac{2}{3}, \frac{1}{12}; 0, 0, \frac{3}{12}; \frac{1}{3}, \frac{2}{3}, \frac{5}{12}; \frac{2}{3}, \frac{1}{3}, \frac{7}{12}; 0, 0, \frac{9}{12}$. The model was checked by comparison with a simulated diffraction pattern map and with a simulated [0001] zone-axis CBED pattern, which showed complete agreement with the proposed model.

Introduction

Laser cladding is attractive because the two materials, the cladding material and the substrate, can be metallurgically bonded to form a composite mechanical component. Extended solid solution of Hf in Ni-based superalloy (Ribaudo, Sircar & Mazumder, 1989), improved wear resistance in Fe–Cr–Mn–C alloys (Singh & Mazumder, 1987) and high-temperature oxidation resistance in Ni–Cr–Al–Hf alloys (Singh, Nagarathnam & Mazumder, 1987) have been achieved by laser cladding. Mechanical components of Ni alloy clad on Al alloy are attractive because of the combined advantages of the high-temperature mechanical properties of the Ni alloy and the light weight of the Al alloy. We were recently successful in laser cladding Ni alloy FP-5 on Al alloy AA333 (Liu, Justin, Mazumder & Shibata, 1994). An intermediate layer of bronze was introduced between the Ni alloy and the Al alloy to toughen the interface (Liu, Mazumder & Shibata, 1994*a*).

Phase identification in laser cladding is critical because: (I) the mechanical properties are closely related to the crystal structure; and (II) brittle intermetallic compounds may be formed at the interface between the cladding and the substrate which makes the interface brittle. The microstructures produced by laser materials processing usually have fine grain size ranging from nanometers to micrometers (Liu, Justin, Mazumder & Shibata, 1994), high-density defects (Liu, Mazumder & Shibata, 1994*b*), local composition fluctuation [the composition may change within a grain (Sircar, Singh & Mazumder, 1989)] and multialloying elements that usually promote the formation of new phases (Liu, Mazumder & Shibata, 1994*c*). X-ray or neutron diffraction techniques are not suitable for structure analysis of laser-processed materials because of diffuse intensity distribution and multiline overlapping in the diffraction data.

Techniques of transmission electron microscopy (TEM) have been employed to identify or determine the crystal structures of phases observed in laser cladding. The crystal structures of several new phases observed in laser cladding were solved by convergent-beam electron diffraction (CBED) and high-resolution electron microscopy (HREM) techniques (Liu, Mazumder & Shibata, 1994*b*,*c*). CBED was used to identify the point group and space group while HREM was used to determine the atomic locations in the unit cell. However, the requirements of HREM for a transmission electron microscope (TEM) specimen are quite strict. For example, the specimen has to be very thin, usually less than 10 nm, to achieve atomic resolution. Also, a proper grain of the phase, which is oriented close to the zone axis to be examined, should be found. It is very desirable that a conventional transmission electron microscope with high-tilt-angle capability is used to solve the crystal structure of an unknown phase. In this paper, we demonstrate an example of solving a simple structure of an unknown phase: the Si-rich phase in laser-clad Ni alloy. The analysis is based on kinematical microdiffraction in the TEM. CBED patterns are used to find the point group and confirm the structure model deduced.

Experimental

An AVCO HPL 10 kW continuous wave CO_2 laser was used for the cladding. The traverse motion was provided by a computer-controlled stepping motor. Direct cladding of Ni alloy on Al alloy created a brittle interface. The cracks at the interface between the clad and the substrate were usually visible to the naked eye. The clad could be easily hammered off the substrate. Two-stage cladding (bronze on Al alloy and Ni alloy on bronze clad layer) was employed to clad Ni alloy onto Al alloy. The compositions of the two cladding powders and the substrate are given in Table 1. First, an overlapping clad layer of bronze about 2 mm thick was laid on the Al alloy. The Ni alloy was then laid on top of the bronze cladding. The processing parameters for cladding bronze on Al alloy were: laser power = 5.3 kW; beam diameter = 4.5 mm; powder feed rate = 47 g min^{-1}; substrate traverse speed = 15.2 mm s^{-1}; assisting gas helium flow = 0.05 m^3 h^{-1}; overlapping percentage of adjacent clads = 55%. For Ni-alloy cladding, an oscillator was connected to the flat mirror and an oscillating frequency of about 100 Hz was used to generate an oscillating width of 8 mm with a laser-beam diameter of 2.5 mm. The cladding parameters for the Ni alloy were: laser power = 2.9 kW; powder feed rate = 27 g min^{-1}; substrate traverse speed = 9.3 mm s^{-1}. More detailed descriptions of laser-cladding processes can be found in papers by Liu, Mazumder & Shibata (1994*a*) and Liu, Justin, Mazumder & Shibata (1994).

TEM specimens cut from the Ni-alloy clad were prepared in three steps. First, 3 mm diameter and 0.2 mm thick discs were prepared by diamond-wheel cutting and standard polishing techniques. These discs were then thinned with a dimpler to about 30 μm thick at the center.

Table 1. *Chemical compositional analysis of the clad material* Ni *alloy FP-5, intermediate layer material* Ni–Al *bronze and* Al *alloy* AA333 (wt%)

	Ni	Cu	Al	Cr	B	Si	C	Fe	Mg	Zn
FP-5	Balance	–	–	11.6	2.33	3.55	0.48	1.99	–	–
Ni–Al bronze	5.27	Balance	9.80	–	–	–	–	2.19	–	–
AA333	0.01	3.14	Balance	0.02	–	8.92	–	0.48	0.30	0.10

Final thinning was done in an ion mill until perforation. The TEM study was performed using a Philips CM12 microscope operating at 120 kV.

Results

The morphology of the Si-rich phase (C5 phase designated in Liu, Justin, Mazumder & Shibata, 1994) is shown in Fig. 1. One example of the TEM EDX spectrum taken from the Si-rich phase is shown in Fig. 2. The peaks are labeled with the corresponding elements. Two typical compositions of TEM EDX analysis are shown in Table 2.

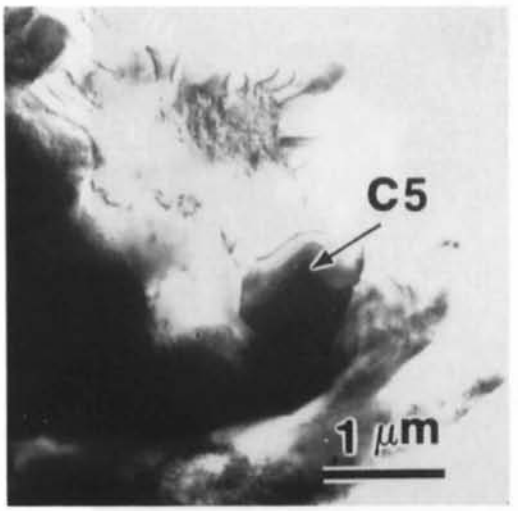

Fig. 1. TEM micrograph showing the morphology of the Si-rich phase.

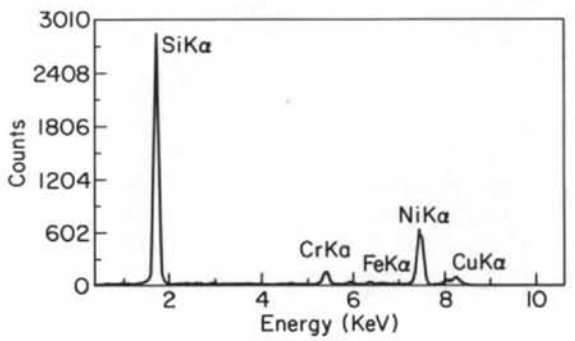

Fig. 2. TEM EDX spectrum of the Si-rich phase.

Table 2. *TEM EDX composition analysis of the* Si*-rich phase* (at.%)

	Al	Si	Cr	Fe	Ni	Cu
1	0.96	81	2.5	0.56	14	1.3
2	0.90	83	2.1	0.45	12	1.4

Table 3. *Observed zone-axis symmetry and deduced diffraction group and point group for the* Si*-rich phase*

Fig. 3	Zone axis	Bright field	Whole pattern	Diffraction group	Point group
(*a*), (*b*)	0001	6*mm*	6*mm*	6*mm*	6*mm*
				$6mm1_R$	6/*mmm*
(*d*)	*hk*l0	2*mm*	2*mm*	2*mm*	*mm*2, $\bar{6}m2$
				$2mm1_R$	*mmm*, 4/*mmm*
					6/*mmm*
					*m*3, *m*3*m*
(*c*)	0001	*G* disc 2*mm*	Discs other than *G* disc *m*	$6mm1_R$	6/*mmm*

A tentative microdiffraction study showed that the structure was not a diamond-structure Si. Structure analysis was then started from symmetry analysis. The CBED patterns of high symmetry taken from the Si-rich phase are shown in Fig. 3 and the symmetry analysis results are summarized in Table 3. The bright-field pattern (Fig. 3*a*) and whole pattern (Fig. 3*b*) clearly show 6*mm* symmetry, which suggests that the structure is hexagonal. The diffraction group and point group were deduced according to Tables II and III of Buxton, Eades, Steeds & Rackham (1976). Generally, more than one diffraction group and point group may be deduced from one zone-axis CBED pattern. Two diffraction groups 6*mm* and $6mm1_R$, corresponding to point groups 6*mm* and 6/*mmm*, respectively, were deduced from Figs. 3(*a*) and (*b*). The difference between point groups 6*mm* and 6/*mmm* is that 6/*mmm* has mirror (this mirror could be a glide plane) symmetry perpendicular to the sixfold axis. Fig. 3(*d*) is a CBED pattern taken near the $[11\bar{2}0]$ zone axis and at 90° from the [0001] zone axis. The pattern serves to check whether the mirror mentioned above exists. Both the bright-field pattern and the whole pattern show 2*mm* symmetry. This proves that the point group is 6/*mmm*. The analysis by Buxton's method is shown in Table 2. Two diffraction groups and seven point groups were deduced from Fig. 3(*d*). The only common point group deduced for Figs. 3(*a*), (*b*) and (*d*) is 6/*mmm*, being consistent with the analysis based on the geographic configuration of the symmetry elements. Tanaka, Sekii & Nagasawa (1983) suggested a symmetry analysis by a symmetrical many-beam method. Fig. 3(*c*) is a symmetrical six-beam pattern of the [0001] zone axis. Comparison with Tanaka *et al.*'s (1983) Table 3 indicates that the pattern matches well with the $6mm1_R$ pattern. Again, the point group 6/*mmm* is deduced.

Since the point group was determined to be 6/*mmm*, which corresponds to a hexagonal unit cell, tilting along

the two mirrors with 30° separation in Fig. 3(*b*) was performed to examine more zone-axis diffraction patterns. Fig. 4 shows major zone-axis diffraction patterns in the [0001], [11$\bar{2}$0] and [10$\bar{1}$0] stereographic triangle. The lattice parameters $a = 3.03$, $c = 14.6$ Å were deduced from the [11$\bar{2}$0] zone-axis pattern. Examination of major zone-axis diffraction patterns indicates that the Si-rich phase is a close-packed structure. In the earlier study, it was shown that the [11$\bar{2}$0] zone-axis diffraction pattern has characteristics of a close-packed structure, *i.e.* the stacking period can be observed in the diffraction pattern (Liu, Mazumder & Shibata 1994*d*). In particular, if the stacking period is N layers, reflections 000l where $l \neq iN$ (i is an integer) have zero structure factors, while reflections 000l where $l = iN$ have large structure factors. The [11$\bar{2}$0] zone-axis pattern taken from TEM is shown in Fig. 5, where (*a*) was taken from a thick area and (*b*) was from a thin area where the intensity is linearly related to structure factors (kinematical). The intensity of spots 000l where $l \neq iN$ is zero as seen in Fig. 5(*b*). These two patterns display the exact features described for the close-packed structure. The stacking period is then easily identified as six.

Next, we deduce the stacking mode of the Si-rich phase. In fact, only two unique stacking modes *ABCACB* and *ABCBCB* can be deduced from the six-layer stacking. Bloch-wave calculation was performed using the *EMS* package (Stadelmann, 1987) to estimate the effect of dynamical scattering. Figs. 5(*c*) and (*d*) are simulated patterns using the selected model *ABCACB* for different thicknesses of 65 and 5 nm, respectively. The double-diffraction routes in the thicker specimen produce the intensity for the spots with zero structure factors. Figs. 5(*e*) and (*f*) are kinematically simulated patterns for stacking mode *ABCBCB* and stacking mode *ABCACB*, respectively. By comparison with the TEM pattern, it is clear that the Si-rich phase has the stacking mode *ABCACB*.

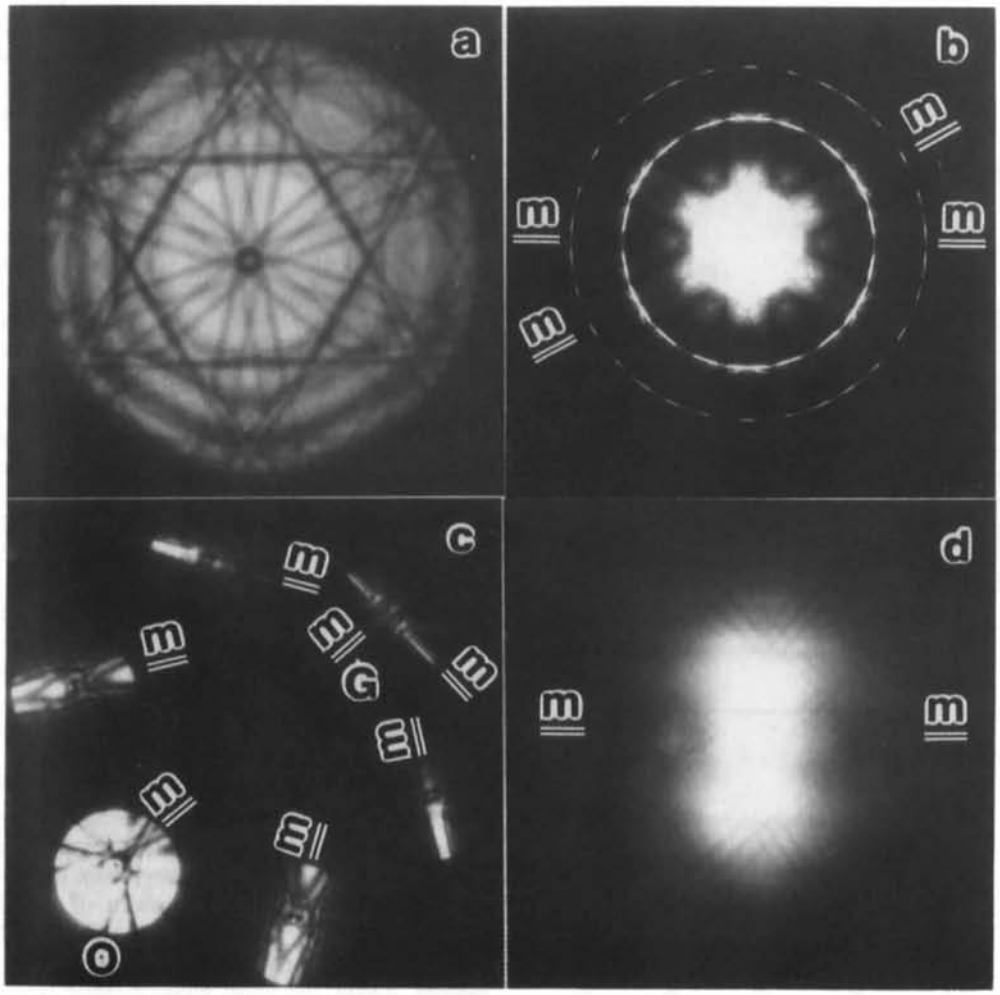

Fig. 3. CBED patterns of the Si-rich phase. (*a*) [0001] bright-field pattern; (*b*) [0001] whole pattern; (*c*) [0001] symmetrical six-beam pattern; (*d*) a pattern 90° from the [0001] zone axis.

Since the stacking modes define the exact positions of the atoms in the unit cell, [0001] zone-axis CBED patterns were simulated for different models to confirm the identified model. The results of the simulation are shown in Fig. 6. The first ten CBED patterns were calculated starting from 50 nm thickness increasing in steps of 20 nm. The correct thickness for the simulated CBED pattern was found by matching to the TEM pattern with a precision of 3 nm. The positions of the HOLZ lines are insensitive to the thickness in the range

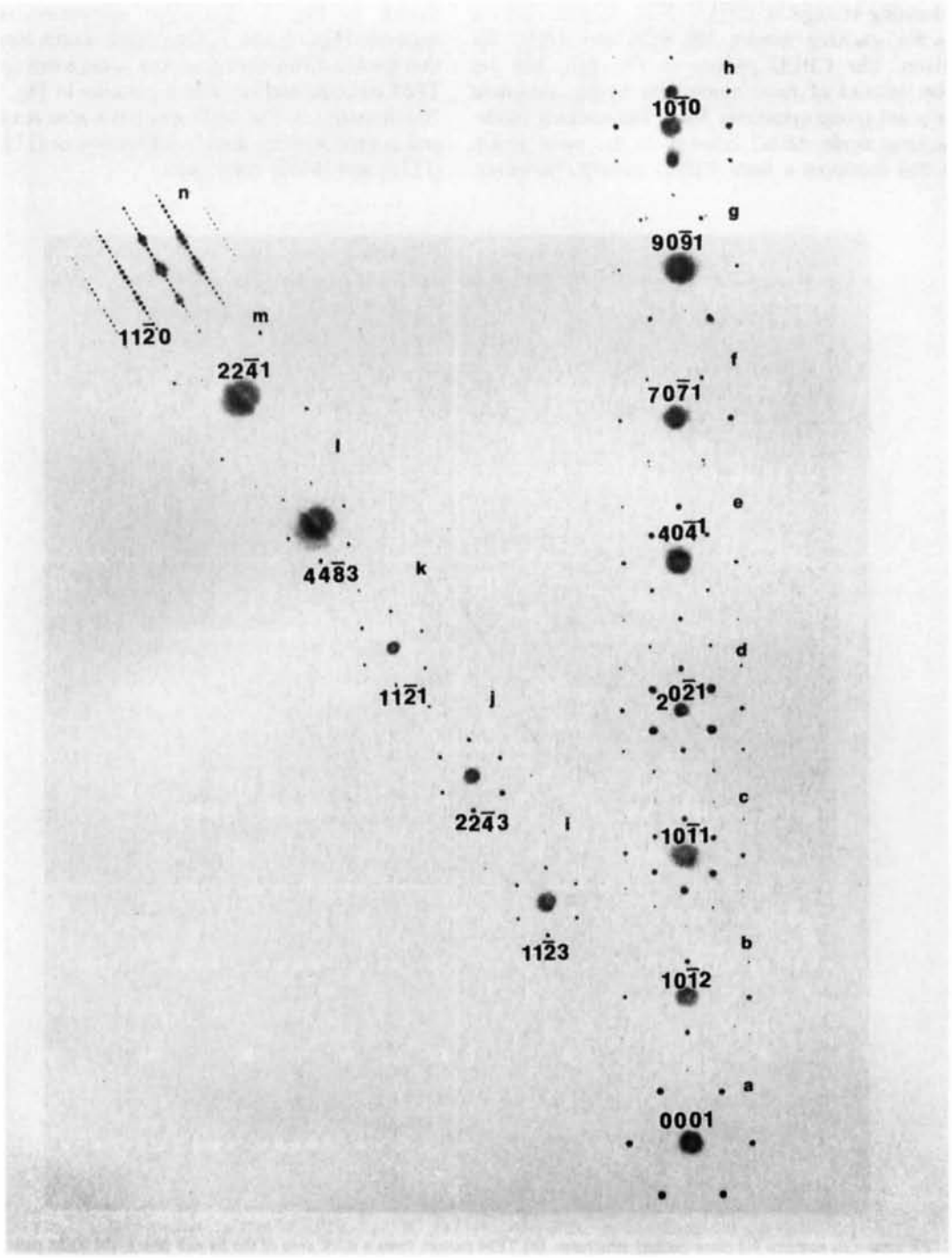

Fig. 4. Diffraction pattern map of the Si-rich phase.

from 130 to 150 nm. The lattice parameters for simulation were adjusted in steps of 0.002 Å for a and 0.02 Å for c until high-order Laue-zone (HOLZ) lines (only the first-order reflections are included here for calculation) in Fig. 6(a) show good agreement with the TEM pattern in Fig. 3(a). Lattice parameters $a = 3.195\,(2)$, $c = 16.45\,(2)$ Å were deduced from Fig. 6(a) assuming an accelerating voltage of 120 kV. Figs. 6(b) and (c) are patterns for stacking modes *ABCBCB* and *ABAC* for comparison. The CBED pattern in Fig. 6(b) has $3m$ symmetry instead of $6mm$ symmetry, being consistent with the point-group symmetry $3m$ of the stacking mode. The stacking mode *ABAC* belongs to the point group $6/mmm$ and produces a $6mm$ CBED pattern. However, the intensities and the positions of the HOLZ lines are different from those for stacking mode *ABCACB*. Therefore, the identification of the right model for the Si-rich phase by the CBED pattern-matching method is decisive.

The stacking mode *ABCACB* was used to produce a diffraction pattern map corresponding to Fig. 4 and is shown in Fig. 7. Excellent agreement is obtained between Figs. 4 and 7. One point worth mentioning is that double diffraction produces some extra spots in both TEM patterns and simulated patterns in Fig. 4 and Fig. 7(i) through (n). The $\bar{1}100$ spot has a zero structure factor and is produced by double diffraction in $[11\bar{2}3]$, $[22\bar{4}3]$, $[11\bar{2}1]$ and $[44\bar{8}3]$ zone axes.

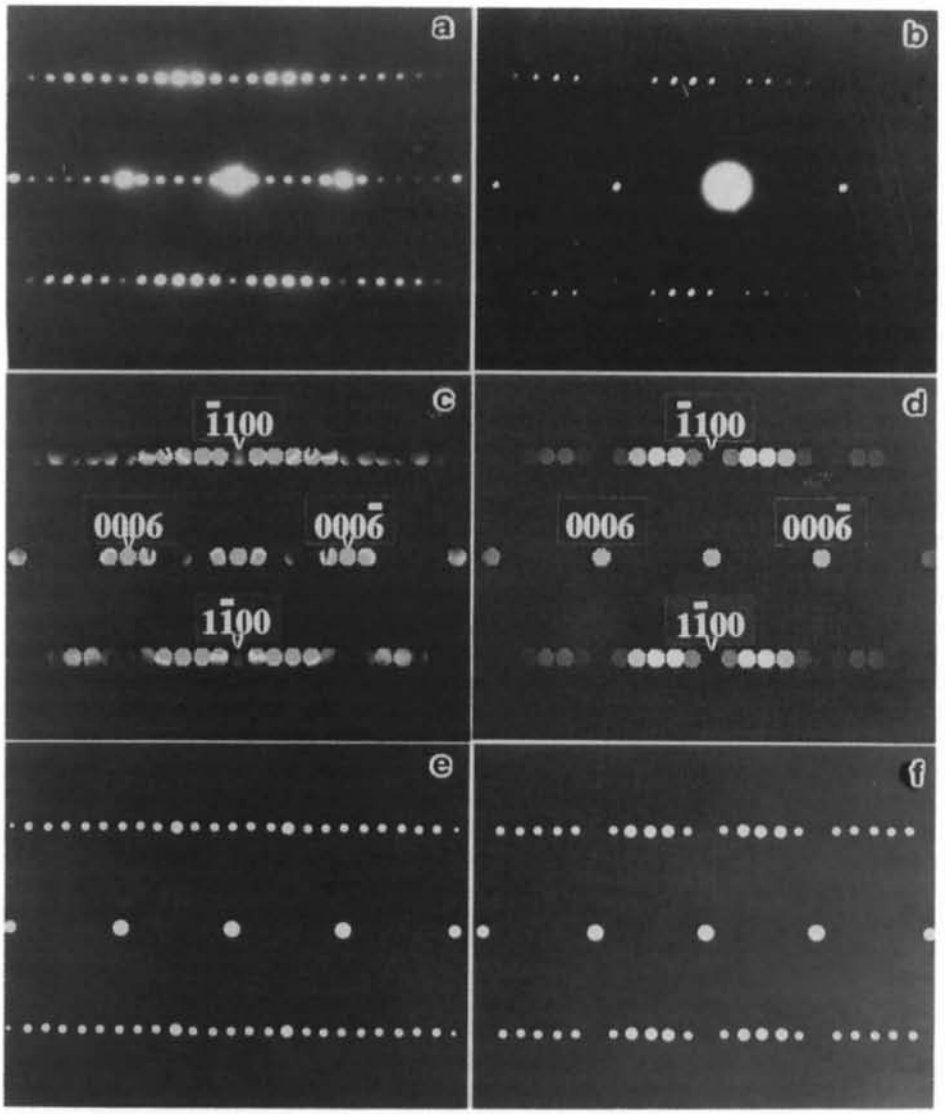

Fig. 5. [1120] zone-axis patterns for close-packed structures. (a) TEM pattern from a thick area of the Si-rich phase; (b) TEM pattern from a thin area of the Si-rich phase; (c) simulated pattern with the stacking model *ABCACB*, thickness = 65 nm; (d) simulated pattern with stacking mode *ABCACB*, thickness = 5 nm; (e), (f) simulated patterns using kinematical theory for models *ABCBCB* and *ABCACB*, respectively.

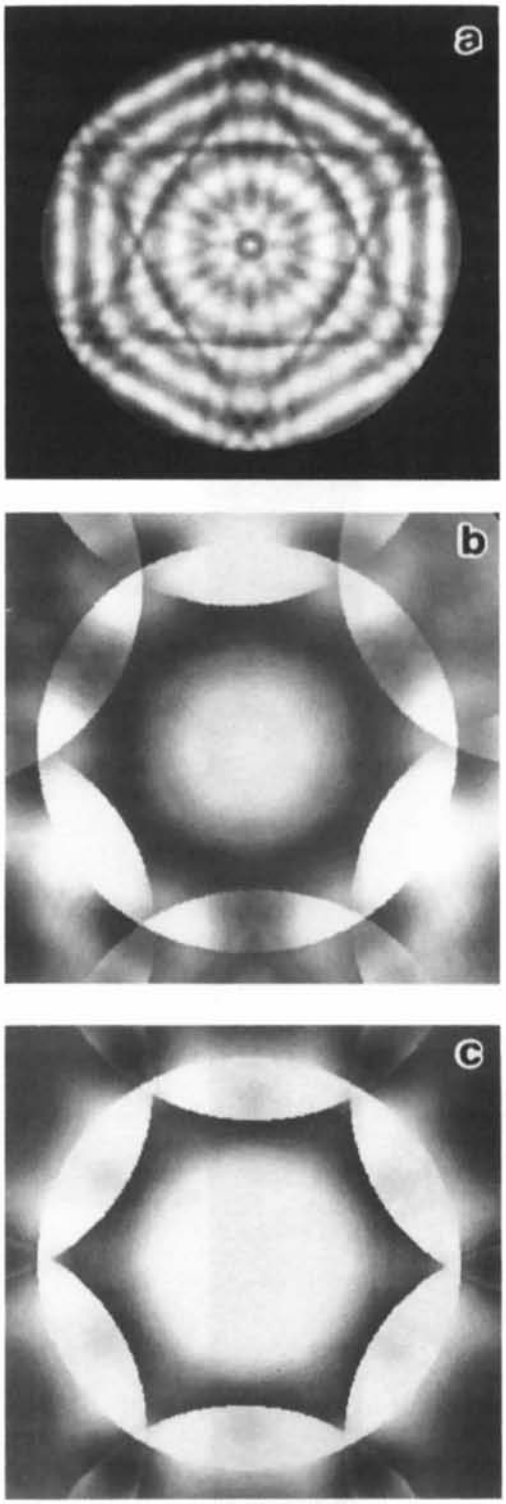

Fig. 6. Simulated [0001] zone-axis bright-field CBED patterns for different stacking modes. (*a*) *ABCACB*, (*b*) *ABCBCB* and (*c*) *ABAC*. Simulation parameters are: accelerating voltage = 120 kV, specimen thickness = 148 nm, beam semiconvergence angle = 2.10 nm^{-1}. Lattice parameters $a = 3.195$, $c = 16.45$ Å were deduced from (*a*) by matching the HOLZ lines with those in Fig. 3(*a*).

Discussion

The space group of the Si-rich phase has not been determined by observing the Gjønnes–Moodie (GM) lines because of limitations to tilting to the exact [11$\bar{2}$0] zone axis ([11$\bar{2}$0] zone-axis patterns in Figs. 4 and 5, which were slightly off zone axis, were taken with maximum *x*-axis tilt). However, as the stacking mode is uniquely determined by microdiffraction and CBED, the space group is indirectly determined. In other words, we can deduce the space group by the atomic coordinates defined by the stacking mode *ABCACB*. There are four space groups, $P6/mmm$, $P6/mcc$, $P6_3/mcm$ and $P6_3/mmc$, in point group $6/mmm$. In each close-packed plane in a close-packed structure, a sixfold axis can only be generated at the position where an atom exists. Since the close-packed structure with six layers must consist of a certain stacking of *A* layers, *B* layers and *C* layers with a shift relative to each other, it is not possible to create a sixfold axis in a close-packed structure consisting of *A*, *B* and *C* layers. The space groups $P6/mmm$ and $P6/mcc$ are therefore eliminated. It turns out that the stacking mode *ABCACB* belongs to space group $P6_3/mmc$ (No. 194), which has a 6_3 screw axis. The stacking mode *ABCACB* can be constructed by filling four atoms at $4(f)$ positions with $z = \frac{1}{12}$ and two atoms at $2(b)$ positions as listed in *International Tables for X-ray Crystallography* (1965). The coordinates for the atoms are $\frac{2}{3}, \frac{1}{3}, -\frac{1}{12}$; $\frac{1}{3}, \frac{2}{3}, \frac{1}{12}$; $0, 0, \frac{3}{12}$; $\frac{1}{3}, \frac{2}{3}, \frac{5}{12}$; $\frac{2}{3}, \frac{1}{3}, \frac{7}{12}$; $0, 0, \frac{9}{12}$.

Pure Si has a diamond structure belonging to space group $Fd3m$ (No. 227). Every Si atom is surrounded by four other Si atoms. The Si–Si atom distance is 2.341 Å. Although the Si-rich phase contains mainly Si and Ni, no similar phases of close-packed structures in the Si–Ni phase diagram are present. Therefore, the formation of the close-packed Si-rich phase must be accounted for by multialloying elements.

With the lattice parameters $a = 3.195$, $c = 16.45$ Å, the interatomic distances are 3.195 Å for atoms within the same close-packed plane and 3.304 Å for the nearest neighbors at adjacent atomic planes. These values are larger than those in cubic diamond Si. However, the volume occupied by each atom is 13.99 $Å^3$, which is smaller than 20.0 $Å^3$ for cubic diamond Si. This volume contraction can be accounted for by two mechanisms: one is that each Si atom in the close-packed structure has 12 nearest neighbors while there are only 4 in the diamond structure; the other is that there are about 17–19 at.% other alloying elements such as Ni, Cr and Fe in the Si-rich phase. The atomic volumes of Cr, Fe and Ni are all much smaller than that of Si. Both mechanisms facilitate lattice contraction.

Summary

The structure of an unknown Si-rich phase of submicrometer size has been solved by combination of

microdiffraction and CBED. The microdiffraction pattern taken on the [11$\bar{2}$0] zone axis with a very thin area has an explicit relation with the stacking period for the close-packed structure while CBED pattern matching provides the most confident verification of the deduced structure model. As a result, the Si-rich phase was determined to be a close-packed structure with the stacking mode *ABCACB*. The steps are summarized as follows.

1. Estimate the composition of the phase by TEM EDX analysis.

2. Establish the point group (and space group) by CBED analysis.

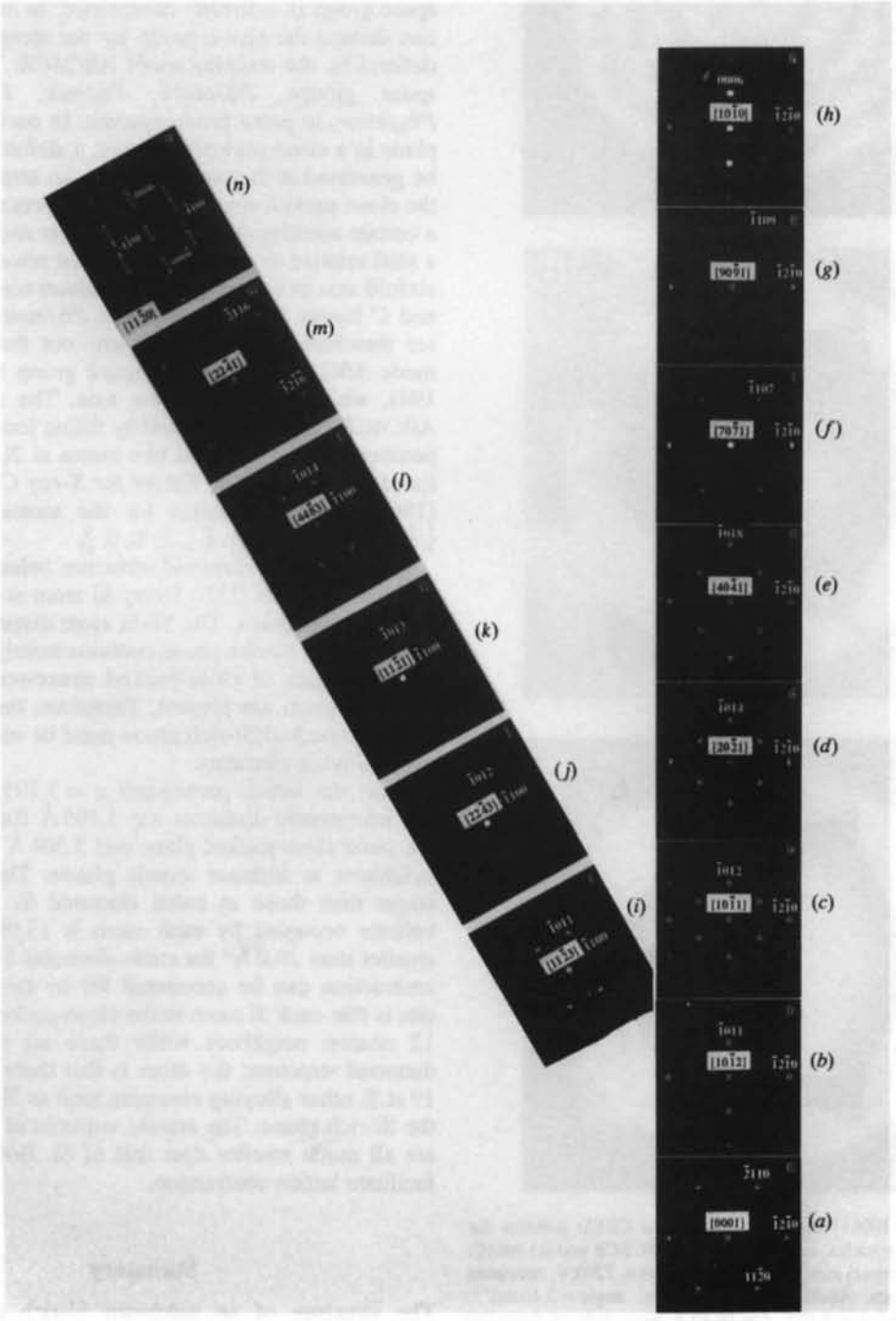

Fig. 7. Simulated diffraction pattern map corresponding to Fig. 4.

3. Make a diffraction pattern map to assist indexing. For the case of the close-packed structure, use the [11$\bar{2}$0] zone-axis microdiffraction pattern to deduce both the stacking period and the stacking sequence. The microdiffraction pattern must be taken in a very thin region to relate the intensity of the diffraction spots to the structure factor.

4. Use the deduced structure model to simulate the CBED pattern and compare it with the TEM pattern. Adjust the lattice parameter until satisfactory agreement is achieved. A well defined CBED pattern is a unique fingerprint of the structure and provides conclusive identification of the structure.

References

BUXTON, B. F., EADES, J. A., STEEDS, J. W. & RACKHAM, G. M. (1976). *Philos. Trans. R. Soc. London*, **281**, 171–194.

International Tables for X-ray Crystallography (1965). Vol. I, pp. 304–305. Birmingham: Kynoch Press.

LIU, Y., JUSTIN, K., MAZUMDER, J. & SHIBATA, K. (1994). *Metall. Trans.* B**25**, 425–434.

LIU, Y., MAZUMDER, J. & SHIBATA, K. (1994*a*). *Metall. Trans.* B**25**, 749–759.

LIU, Y., MAZUMDER, J. & SHIBATA, K. (1994*b*). *Acta Metall.* **42**, 1755–1762.

LIU, Y., MAZUMDER, J. & SHIBATA, K. (1994*c*). *Metall. Trans.* A**25**, 487–497.

LIU, Y., MAZUMDER, J. & SHIBATA, K. (1994*d*). *Metall. Trans.* A**25**, 37–46.

RIBAUDO, C., SIRCAR, S. & MAZUMDER, J. (1989). *Metall. Trans.* A**20**, 2489–2497.

SINGH, J. & MAZUMDER, J. (1987). *Acta Metall.* **35**, 1995.

SINGH, J., NAGARATHNAM, K. & MAZUMDER, J. (1987). *High Temp. Tech.* **5**, 131–137.

SIRCAR, S., SINGH, J. & MAZUMDER, J. (1989). *Acta Metall.* **37**, 1167–1176.

STADELMANN, P. A. (1987). *Ultramicroscopy*, **21**, 131–146.

TANAKA, M., SEKII, H. & NAGASAWA, T. (1983). *Acta Cryst.* A**39**, 825–837.

Acta Cryst. (1995). A**51**, 489–497

Hexamethylenetetramine: Extinction and Thermal Vibrations from Neutron Diffraction at Six Temperatures

BY S. P. KAMPERMANN, T. M. SABINE* AND B. M. CRAVEN†

Department of Crystallography, University of Pittsburgh, Pittsburgh, PA 15260, *USA*

AND R. K. MCMULLAN

Department of Chemistry, Brookhaven National Laboratory, Upton, NY 11973, *USA*

(*Received* 25 *March* 1994; *accepted* 28 *November* 1994)

Abstract

Neutron diffraction data have been collected for hexamethylenetetramine (HMT) at 15, 50, 80, 120, 160 and 200 K using a single crystal (mass 8.1 mg). The structure refinement at each temperature included two extinction parameters and third-order thermal parameters for the H nuclei. Extinction effects are very severe with extinction factors as small as $0.2F^2_{kin}$ for three reflections (800, 110 and 440). Application of the Sabine extinction theory indicates that the crystal domain size decreases from 115 μm at 200 K to 85 μm at 15 K. The half-width in the mosaic spread (7″ of arc) is almost independent of temperature. An extinction model without phase correlations between mosaic blocks gives a slightly better fit to the diffraction data. The nuclear mean square thermal displacements have been analysed assuming no coupling between the external (rigid body) and internal vibrations. This gives mean square displacements for rigid-body vibration in which zero-point vibrational effects are apparent. The methylene H nuclei have internal vibrations approximately independent of temperature. At 200 K, the H nuclear vibrations have a small anharmonic component, but at temperatures below 160 K this becomes insignificant in terms of the experimental error.

Introduction

The crystal structure of hexamethylenetetramine (HMT, $C_6H_{12}N_4$; Fig. 1) was first determined by Dickinson & Raymond (1923). Much of the interest in this molecular crystal structure comes from its simplicity and high symmetry. The $\bar{4}3m$ molecular point symmetry is fully utilized in the crystal that has space group $I\bar{4}3m$ with two molecules per cell. Thus, the asymmetric unit consists of

* Permanent address: Australian Nuclear Science and Technology Organization, Lucas Heights, NSW, Australia.

† Author for correspondence.